

# On the nature and evolution of the unique binary pulsar J1903+0327

P. C. C. Freire<sup>1</sup>, C. G. Bassa<sup>2</sup>, N. Wex<sup>1</sup>, I. H. Stairs<sup>3</sup>, D. J. Champion<sup>1</sup>,  
S. M. Ransom<sup>4</sup>, P. Lazarus<sup>5</sup>, V. M. Kaspi<sup>5</sup>, J. W. T. Hessels<sup>6,7</sup>, M. Kramer<sup>1</sup>,  
J. M. Cordes<sup>8</sup>, J. P. W. Verbiest<sup>1,9</sup>, P. Podsiadlowski<sup>10</sup>, D. J. Nice<sup>11</sup>, J. S. Deneva<sup>12</sup>,  
D. R. Lorimer<sup>9,13</sup>, B. W. Stappers<sup>2</sup>, M. A. McLaughlin<sup>9,13</sup> and F. Camilo<sup>14</sup>

<sup>1</sup> *Max-Planck-Institut für Radioastronomie, Auf dem Hügel 69, D-53121 Bonn, Germany*

<sup>2</sup> *Jodrell Bank Centre for Astrophysics, Univ. of Manchester, Oxford Rd, Manchester, M13 9PL UK*

<sup>3</sup> *Dept. of Physics and Astronomy, Univ. of British Columbia, 6224 Agricultural Rd., Vancouver, BC V6T 1Z1, Canada*

<sup>4</sup> *National Radio Astronomy Observatory, 520 Edgemont Rd., Charlottesville, VA 22903, USA*

<sup>5</sup> *Dept. of Physics, McGill Univ., Montreal, QC H3A 2T8, Canada*

<sup>6</sup> *Netherlands Institute for Radio Astronomy (ASTRON), Postbus 2, 7990 AA Dwingeloo, The Netherlands*

<sup>7</sup> *Astronomical Institute “Anton Pannekoek,” Univ. of Amsterdam, 1098 SJ Amsterdam, The Netherlands*

<sup>8</sup> *Dept. of Astronomy, Cornell Univ., Ithaca, NY 14853, USA*

<sup>9</sup> *Dept. of Physics, West Virginia Univ., Hodges Hall, Morgantown, WV 26506-6315, USA*

<sup>10</sup> *Dept. of Astronomy, Oxford Univ., Oxford OX1 3RH, UK*

<sup>11</sup> *Dept. of Physics, Lafayette College, Easton, PA 18042, USA*

<sup>12</sup> *Arecibo Observatory, HC 3 53995, Arecibo, PR 00612, USA*

<sup>13</sup> *National Radio Astronomy Observatory, Green Bank, WV 24944, USA*

<sup>14</sup> *Columbia Astrophysics Laboratory, Columbia Univ., 550 West 120th St., New York, NY 10027, USA*

Re-submitted version

## ABSTRACT

PSR J1903+0327, a millisecond pulsar in an eccentric ( $e = 0.44$ ) 95-day orbit with a ( $\sim 1 M_{\odot}$ ) companion poses a challenge to our understanding of stellar evolution in binary and multiple-star systems. Here we describe optical and radio observations which rule out most of the scenarios proposed to explain formation of this system. Radio timing measurements of three post-Keplerian effects yield the most precise measurement of the mass of a millisecond pulsar to date:  $1.667 \pm 0.021$  solar masses (99.7% confidence limit). This rules out some equations of state for super-dense matter, furthermore it is consistent with spin-up of the pulsar by mass accretion, as suggested by its short spin period and low magnetic field. Optical spectroscopy of a proposed main sequence counterpart show that its orbital motion mirrors the pulsar’s 95-day orbit; being therefore its binary companion. This finding rules out a previously suggested scenario which proposes that the system is presently a hierarchical triple. Conventional binary evolution scenarios predict that, after recycling a neutron star into a millisecond pulsar, the binary companion should become a white dwarf and its orbit should be nearly circular. This suggests that if PSR J1903+0327 was recycled, its present companion was not responsible for it. The optical detection also provides a measurement of the systemic radial velocity of the binary; this and the proper motion measured from pulsar timing allow the determination of the systemic 3-D velocity in the Galaxy. We find that the system is always within 270 pc of the plane of the Galaxy, but always more than 3 kpc away from the Galactic centre. Thus an exchange interaction in a dense stellar environment (like a globular cluster or the Galactic centre) is not likely to be the origin of this system. We suggest that after the supernova that formed it, the neutron star was in a tight orbit with a main-sequence star, the present companion was a tertiary farther out. The neutron star then accreted matter from its evolving inner MS companion, forming a millisecond pulsar. The former donor star then disappears, either due to a chaotic 3-body interaction with the outer star (caused by the expansion of the inner orbit that necessarily results from mass transfer), or in the case of a very compact inner system, due to ablation/accretion by the newly formed millisecond pulsar. We discuss in detail the possible evolution of such a system before the supernova.

**Key words:** pulsars: general — pulsars: searches — pulsars: timing — stars: neutron

## 1 INTRODUCTION

PSR J1903+0327 was the first millisecond pulsar (MSP<sup>1</sup>) discovered in the ongoing Arecibo L-band Feed Array (ALFA) pulsar survey Cordes et al. (2006). In the discovery paper Champion et al. (2008), we presented the results of phase-coherent radio timing of this pulsar carried out with the Green Bank and Arecibo radio telescopes. These quickly revealed that the pulsar was in a 95-day orbit around a 1 solar mass ( $M_{\odot}$ ) companion. This object is remarkable for being the first (and thus far, the only) disk MSP known to have an eccentric ( $e = 0.44$ ) orbit. In globular clusters (GCs) there are several binary MSPs with eccentric orbits; but those are thought to be caused by perturbations of the binary systems by occasional close interactions with other stars.

Coincident with the pulsar position derived from the timing, a star was found whose near-infrared magnitudes were consistent with a  $1 M_{\odot}$  main-sequence star at the distance and reddening estimated for PSR J1903+0327. It was not known then whether this was just an unlikely ( $\sim 2.6\%$ ) chance alignment or whether the star is genuinely associated with PSR J1903+0327, and if so whether it is the binary companion responsible for the 95-day orbit of the pulsar. Such a finding would be surprising, as the conventional understanding of MSP evolution posits that such a neutron star (NS) is spun up to high spin frequencies by accretion of matter and angular momentum from a companion star while the companion passes through a giant phase Bhattacharya & van den Heuvel (1991); this circularises the system, and a recycled MSP is left orbiting a low-mass white dwarf (the remnant core of the donor) in a low-eccentricity orbit ( $e < 10^{-3}$ ; Phinney 1992). Until the discovery of PSR J1903+0327 all known MSPs in the Galactic disk had such low-eccentricity orbits. For reviews, see Phinney & Kulkarni (1994), Stairs (2004), Tauris & van den Heuvel (2006).

For these reasons, Champion et al. (2008) proposed that PSR J1903+0327 may be part of a triple system where the 95-day orbit of the pulsar is caused by a massive unseen WD and the third member is the star detected in the near-infrared. The latter is in a long-period orbit and drives the eccentricity of the inner pair through the Kozai mechanism Kozai (1962). An alternative possibility, also discussed in Champion et al. (2008) is that the companion to PSR J1903+0327 in the 95-day orbit is the star detected in the near-infrared, but that this eccentric, unusual system originated in an exchange interaction in a dense stellar environment, like a globular cluster.

In this paper, we present new optical measurements and further radio timing of PSR J1903+0327 obtained with the aim of testing these scenarios. The plan for the rest of this paper is as follows. The optical and radio observations are described § 2. The immediate results from these observations are described in § 3. In § 4 we discuss the implications of these results regarding the formation and evolution of this system. In § 5 we discuss how this system might have formed. We summarise our main conclusions in § 6.

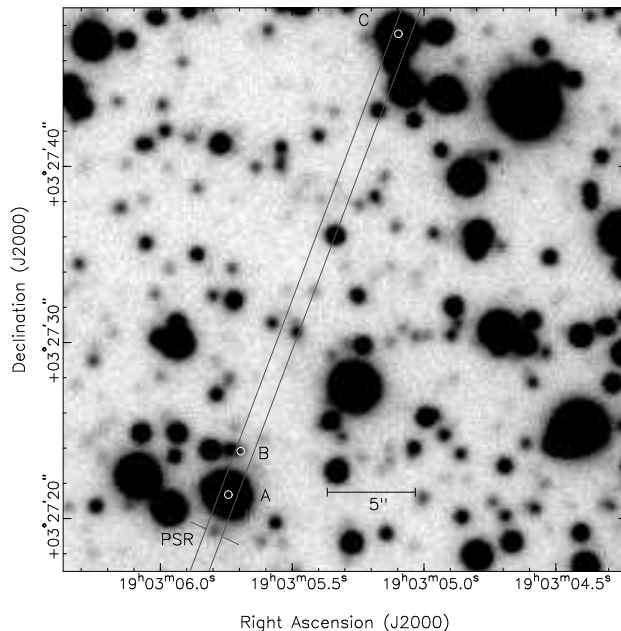


**Figure 1.** This  $32'' \times 32''$  subsection of a 5 min SDSS *i*-band image taken with GMOS at Gemini North on Sept. 20th, 2007 shows the location of the  $1''$  slit. Besides the companion to PSR J1903+0327 denoted with 'PSR', spectra were also extracted of stars A, B and C.

## 2 OBSERVATIONS

### 2.1 Optical observations

Long-slit spectroscopy of the suspected counterpart to PSR J1903+0327 was obtained with FORS2 Appenzeller et al. (1998), the low dispersion spectrograph of ESO's Very Large Telescope. Four spectra were obtained on 2008 June 21, three on 2008 August 23 and one a day later, on August 24. All spectra had exposure times of 46 minutes, and used a  $1''$  slit combined with the 1028Z holographic grism, providing wavelength coverage over  $7830 \text{ \AA}$  to  $9570 \text{ \AA}$ . The detectors were read out with  $2 \times 2$  binning, yielding a resolution of  $3.4 \text{ \AA}$ , sampled at  $0.86 \text{ \AA pix}^{-1}$ . The slit was placed such that both the pulsar companion and a bright nearby star were centred on the slit. The observations were taken during clear and photometric nights, with the seeing between  $0''.48$  and  $0''.72$ . The spectral observations were corrected for bias and flat-fielded using lamp flats.

Spectral extraction is complicated by the bright star, henceforth star A, located  $2''.3$  from the pulsar counterpart (see Fig. 2.1). The star is brighter by about 5.6 mag in the *I*-band and as a result about 20% of the detected counts at the spatial position of the pulsar counterpart are from the wings of the brighter star. The regular optimal extraction algorithm as described by Horne (1986) is not suited to extract blended spectra as it makes no assumptions about the spatial profile. Instead, we use a variation on the algorithm by Hynes (2002), which is based on the optimal extraction method of Horne (1986).

Hynes (2002) uses an analytic function to describe the spatial profile as a function of wavelength. This profile is fitted to the spectrum of an isolated template source and then

<sup>1</sup> We define a millisecond pulsar as a pulsar with spin period  $P \leq 20 \text{ ms}$  and with a low surface magnetic field,  $B \sim 10^{8-9} \text{ G}$ .

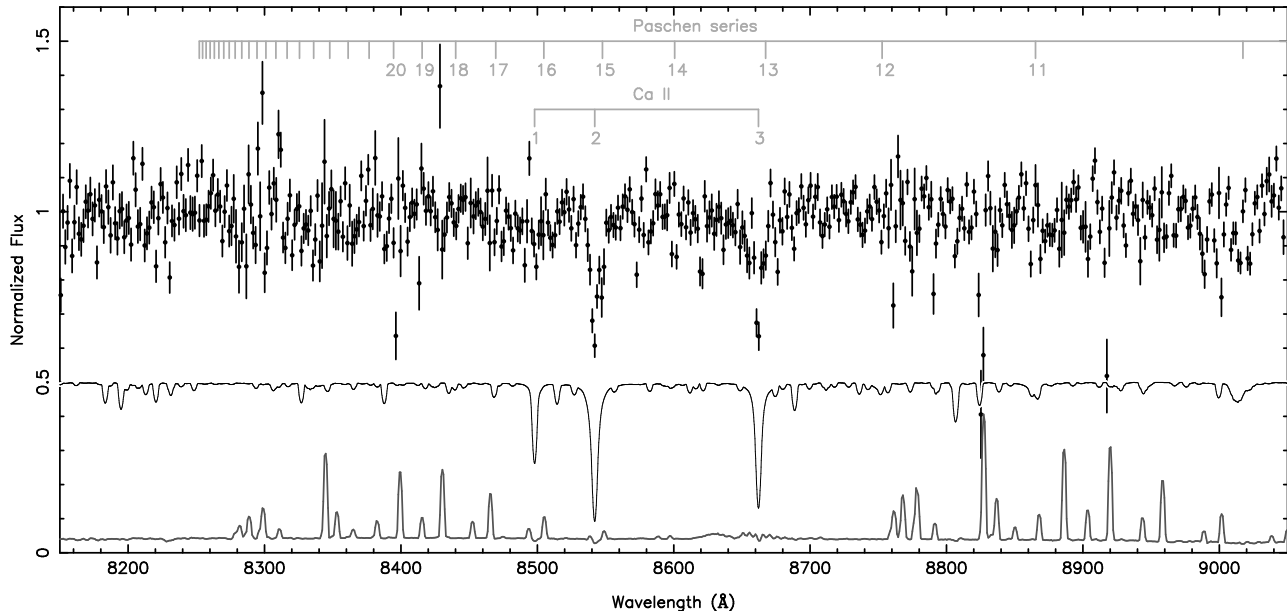


**Figure 2.** The spectrum of the counterpart of PSR J1903+0327. Shown with error bars are the average data from the 8 individual spectra, normalised, shifted to zero velocity and binned by a factor of 2. The best fit normalised spectrum from the library of Munari et al. (2005) is shown as the solid black line, shifted downwards by 0.5 units. The average night sky emission spectrum is shown by the solid grey line, showing the location of emission lines as regions of reduced sensitivity. The vertical scale is arbitrary. The location of stellar absorption lines belonging to the Ca II triplet and the Paschen series of Hydrogen are denoted in grey above the spectrum.

used to simultaneously extract the spectra of the blended sources. We use a variation on this method. First, instead of using a Voigt function to describe the spatial profile we use a Moffat (1969) function, essentially a modified Lorentzian with a variable exponent. Secondly, instead of removing the sky contribution before extraction, we include it in the fit, representing the sky as a first order polynomial added to the Moffat profiles for each object in the blend. Finally, the absence of an isolated template source forced us to use star A as a template. We used an iterative scheme to converge the properties of the profile as a function of wavelength from star A while removing the contribution of the pulsar counterpart and another faint star (star B) that was also part of the blend. In addition to these three objects, a fourth star (star C) is located  $28''$  North-West of PSR J1903+0327 on the slit. This star was not blended and extracted normally.

Arc lamp exposures obtained during daytime with the telescope pointing towards the zenith were used for wavelength calibration. However, comparison of wavelengths of the night sky emission lines from the science exposures showed wavelength offsets of up to  $0.8 \text{ \AA}$  between different exposures, most likely due to flexure caused by the telescope pointing away from zenith. To correct for these offsets the wavelength calibration of June 21st was used to create a secondary line list of some 60 night sky emission lines in the first spectrum, which was subsequently used to calibrate the remaining 7 spectra. Typical rms residuals of these fits were less than  $0.05 \text{ \AA}$ .

Figure 2 shows the averaged spectrum of the counterpart to PSR J1903+0327. The spectrum has a signal-to-noise ratio (S/N) of 15 to 20 in the wavelength range of  $8000 \text{ \AA}$  to  $9000 \text{ \AA}$ . The spectrum is generally featureless except for clear absorption lines around  $8540 \text{ \AA}$  and  $8660 \text{ \AA}$ . At these wavelengths the most common spectral lines are

those belonging to the Ca II triplet, and the Paschen series of Hydrogen (see Cenarro et al. 2001). Though the Paschen series has lines on these wavelengths, the absence of the other lines in the series argues for them being due to the Calcium triplet.

## 2.2 Radio timing observations

We made pulse time of arrival (TOA) measurements of PSR J1903+0327 using the 305-m Arecibo radio telescope and the 105-m Green Bank Telescope from 2006 December through 2010 January; the observation dates and radio frequencies are summarised in Fig. 3. The TOAs obtained before 2008 January were described and used by Champion et al. (2008). We now describe the observational setups used at the two observatories.

In this re-analysis we use all the TOAs obtained from processing of data taken with the Green Bank S-band receiver (with frequency coverage from 1650 to 2250 MHz); these cover most of the year 2007. The data were acquired using the “Spigot” pulsar backend — a 3-level autocorrelation spectrometer which samples observing bands of up to 800 MHz Kaplan et al. (2005). Autocorrelation functions (ACFs) of length 2048 lags were accumulated with 3-level precision and written to disk every  $81.92 \mu\text{s}$ . The ACFs were subsequently Fourier transformed to synthesise 2048-channel power spectra. We separately analyzed the lower and upper half of the band, dedispersing each and deriving TOAs using the methods described in the Supplement of Champion et al. (2008). The TOA uncertainties are  $6 \mu\text{s}$  in the upper half and  $10 \mu\text{s}$  in the lower half of the band. In Champion et al. (2008), only data from the upper half of the band were used.

The Arecibo data were obtained with four Wideband

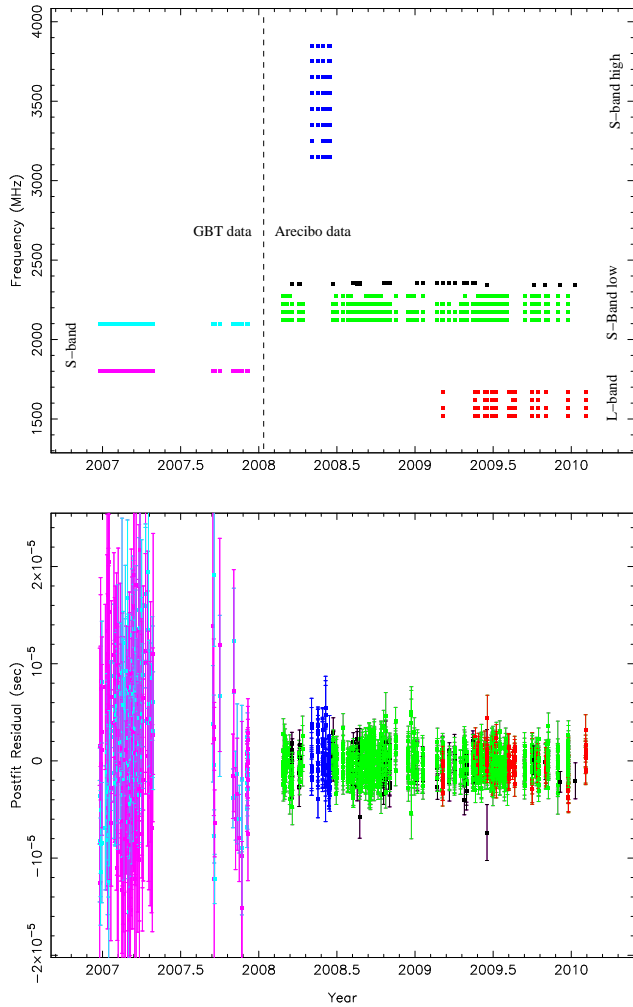


**Figure 3.** *Top:* TOA frequencies versus time (in years). *Bottom:* Post-fit TOA residuals versus time (in years). The different colours indicate different observing systems. *Light Blue:* Green Bank SPIGOT data, centred at 2100 MHz, *Pink:* Green Bank SPIGOT data, centred at 1800 MHz. This was not previously taken into account. *Dark blue:* Arecibo WAPP data taken with the “S-high” receiver. *Light Green:* Arecibo WAPP data taken with the “S-wide” receiver. *Red:* Arecibo WAPP data taken with the “L-wide” receiver. *Black:* Arecibo ASP data (also taken with the “S-wide” receiver).

Arecibo Pulsar Processors (WAPPs; Dowd, Sisk & Hagen, 2000). With the “L-wide” receiver, the WAPPs had bandwidth 50 MHz and were centred at 1520, 1570, 1620 and 1670 MHz; each produced 512-lag ACFs sampled with 3-level precision, accumulated and integrated every  $64\mu\text{s}$ . With the “S-wide” receiver, the WAPPs had bandwidth 50 MHz and were centred at 2125, 2175, 2225, and 2275 MHz, though the latter was sometimes disconnected in order to use the Arecibo Signal Processor (ASP, described below) in its place. At these frequencies, the WAPPs produced 256-lag ACFs which were integrated for  $32\mu\text{s}$ . With the ‘S-high’ receiver, the WAPPs were configured in dual-board mode, allowing 100 MHz of bandwidth in each of 8 correlator boards, centred at 100 MHz intervals from 3150 to 3850 MHz. Each board produced 128-lag ACFs integrated for  $32\mu\text{s}$ .

As for the Spigot data, the ACFs from the WAPPs are Fourier transformed to produce power spectra. These data were then dedispersed and folded modulo the pulsar’s period using a routine written by one of us (IHS) specifically for this purpose; this folds the spectra using polynomial coefficients calculated specifically for the specified observing frequencies. The folding results in 128-bin pulse profiles every 500 seconds for each WAPP.

During some of the S-wide observations we collected data with the Arecibo Signal Processor (ASP, Demorest 2007) in parallel with three WAPPs. The ASP band had a centre frequency of 2350 MHz. The ASP coherently dedisperses a maximum of 16 4-MHz bands, for a maximum bandwidth of 64 MHz. These data were then immediately folded at the pulsar’s rotational period, and 512-bin pulse profiles were stored for each of these bands every 120 seconds. However, because of the large dispersion measure (DM) of PSR J1903+0327 we can only coherently dedisperse 12 of these 4-MHz bands at any given time. Finally, we add all the bands and four 120-s integrations to produce pulse profiles with good S/N.

All pulse profiles are cross-correlated in the Fourier domain Taylor (1992) with a low-noise template derived from the sum of the pulse profiles obtained with the same spectrometer and at the same frequency. From this, we derive a total of 1872 topocentric TOAs. Both the high-resolution WAPP and ASP data provide TOA measurements with an average uncertainty of  $\sim 1\mu\text{s}$ .

In the next step we use the TEMPO2 software package (Hobbs et al. 2006) for TOA analysis. This applies the clock corrections intrinsic to the observatory, the Earth rotation data and the observatory coordinates to convert the TOAs to Terrestrial Time (TT), as maintained by the Bureau International des Poids et Mesures. For conversion of TT TOAs to Coordinated Barycentric Time (TCB) TOAs we used the DE/LE 421 solar system ephemeris (Folkner, Williams & Boggs, 2008). The program then minimises the squares of TOA residuals — the difference between the observed and predicted TOAs. We used the “DD” orbital model Damour & Deruelle (1985, 1986); this is optimal for describing eccentric orbits in a theory-independent manner. The best-fit parameters are listed in Table 1, their uncertainties are the  $1-\sigma$  values estimated by TEMPO2 (throughout this paper, the quoted uncertainties are  $1-\sigma$ , except when stated otherwise). The TOA residuals are displayed in the bottom plot of Fig. 3.

We have performed a parallel analysis using the TEMPO software package<sup>2</sup>. The resulting timing parameters and their uncertainties (as estimated by TEMPO) are also presented in Table 1. Several timing parameters are different from those estimated by TEMPO2. All time-like quantities (spin frequency, orbital period, projected semi-major axis, time of passage through periastron and  $\omega$ , which is strongly covariant with the latter) are different because TEMPO converts the TOAs to Barycentric Dynamic Time (TDB), a time scale that is different from TCB. The right ascension and declination are different because the DE/LE 405 solar system ephemeris Standish (1998) uses an earlier celestial reference frame. Furthermore, we included in TEMPO a mod-

<sup>2</sup> <http://sourceforge.net/projects/tempo/>

ified version of the DD orbital model that uses the orthometric parameterization of the Shapiro delay, as described in Freire & Wex (2010). The “orthometric amplitude” ( $h_3$ ) and the “orthometric ratio” ( $\varsigma$ ) provide an improved description of the areas of the  $(m_c, \sin i)$  plane where the system is likely to be compared to the “range” ( $r$ ) and “shape” ( $s$ ) parameters used in the normal parameterization. In cases where we can measure other post-Keplerian (PK) parameters, the new parameterization yields an improved test of general relativity.

Using either TEMPO or TEMPO2 there are no apparent trends in the residuals and the normalised  $\chi^2$  is 1.3, which is similar to what we observe in other MSPs timed with these observing systems. This means that the timing model provides a complete description of the observed TOAs, with no significant, unmodelled effects present. This also means that the  $1\text{-}\sigma$  uncertainties reported by TEMPO and TEMPO2 are reasonably accurate estimates of the real uncertainties. The non-unity value of the normalised  $\chi^2$  likely reflects a slight underestimation of the TOA uncertainties by the cross-correlation analysis, but it could also be due to red noise in the pulsar rotation, as suggested by the marginal (almost  $3\text{-}\sigma$ ) detection of  $\dot{\nu}$ . To account for this, the timing parameters in Table 1 were obtained after the multiplication of the TOA uncertainty estimates by a scale factor; this is calculated separately for each dataset so that its normalised  $\chi^2$  is 1. This scale factor is 1.1 for all the Arecibo data and 1.3 for the GBT data.

### 3 RESULTS

#### 3.1 On the nature of the companion

Radial velocities and spectral parameters were determined by comparing the observed spectra, both individual and averages at each epoch, with synthetic spectral templates from the spectral library of Munari et al. (2005). These models range in effective temperature  $T_{\text{eff}}$ , surface gravity  $g$ , rotational velocity  $V_{\text{rot}}$  and metallicity  $[M/H]$  and are sampled at a resolution of  $\lambda/\Delta\lambda = 20000$ . The wavelength range between  $8400\text{ \AA}$  and  $8800\text{ \AA}$  was used. To remove the effects of the finite resolution of the instrument, the synthetic spectra were convolved with a Gaussian profile with a width equal to the seeing, and truncated at the width of the slit. For each object, an iterative procedure was used to first determine the radial velocities using a starting template, then use those velocities to shift all spectra to zero velocity and create an average which was then used to obtain a better matching template for determining more accurate radial velocities.

The comparison of the average spectrum with synthetic spectra from the library of Munari et al. (2005) yields a temperature of  $T_{\text{eff}} = 5825 \pm 200\text{ K}$  ( $1\sigma$ ) and sets a  $2\text{-}\sigma$  lower limit on the surface gravity of  $\log g > 4\text{ cm s}^{-2}$ , firmly excluding the possibility of a giant or sub-giant star (see Fig. 4). Based on the shape of the absorption lines we estimate a  $3\text{-}\sigma$  upper limit on the rotational broadening of  $v_{\text{rot}} \sin i_* < 140\text{ km s}^{-1}$ , where  $i_*$  is the inclination of the star. The observed spectrum does not constrain the metallicity. Stellar evolution models Girardi et al. (2000) show that a main sequence (MS) star with the observed mass and effective temperature of the companion of PSR J1903+0327

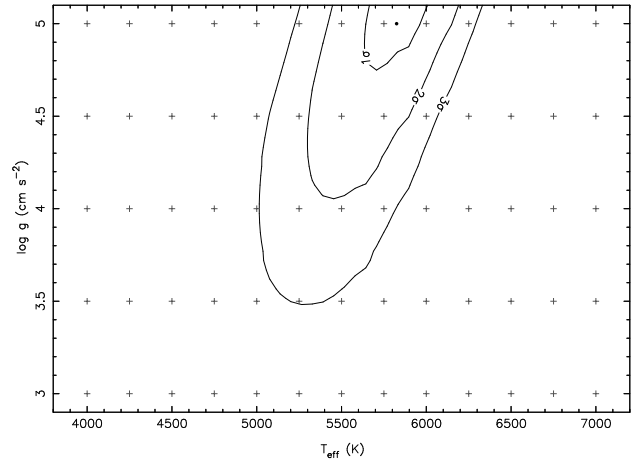


**Figure 4.** Confidence contours for the effective temperature ( $T_{\text{eff}}$ ) and surface gravity [ $\log(g/\text{cm s}^{-2})$ ] for the companion of PSR J1903+0327.

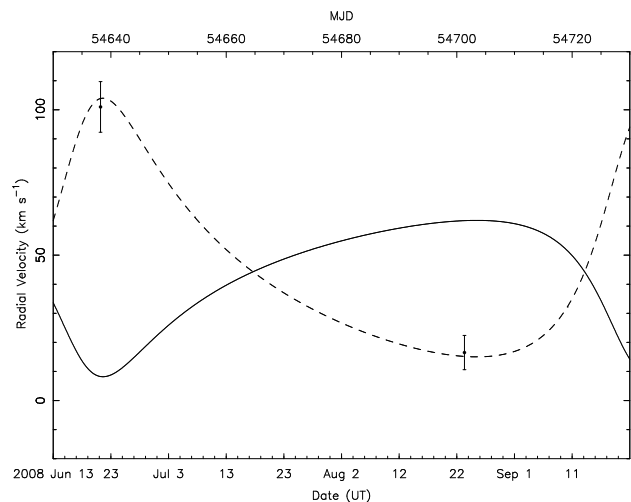


**Figure 5.** The predicted radial velocities of the pulsar (solid line) and companion (dashed line) based on the pulsar timing ephemeris. These are vertically offset by the systemic radial velocity of the system relative to the solar system barycentre  $\gamma$ , which cannot be determined from the radio measurements. The two optical radial velocity measurements are shown with their error bars. Their difference is consistent with the predictions from the pulsar timing ephemeris, and their absolute values allow an estimate of  $\gamma = 44.3 \pm 4.9\text{ km s}^{-1}$ .

is consistent with the observed infrared colours for distances between 6 and 8 kpc, assuming the estimated reddening as a function of distance from 2MASS stars Champion et al. (2008). This is in agreement with the 6.4 kpc distance estimated from the pulsar’s DM (see Table 1) using the Cordes & Lazio (2002) model of the Galactic electron distribution. The predicted ages from these models range from 4 to 7 Gyr.

#### 3.2 Radial Velocities

Table 2 shows the radial velocities of the pulsar counter-part relative to the Solar System barycentre. They are  $V_1 = 92.4 \pm 8.3\text{ km s}^{-1}$  during the first epoch, and  $V_2 =$

Timing parameters		
Timing Program	TEMPO	TEMPO2
Solar System Ephemeris	DE 405/LE 405	DE 421/LE 421
Reference Time Scale	TDB	TCB
Orbital Model	Modified DD	DD
Reference Time (MJD)	55000	55000
Right Ascension, $\alpha$ (J2000)	19 <sup>h</sup> 03 <sup>m</sup> 05 <sup>s</sup> .793296(2)	19 <sup>h</sup> 03 <sup>m</sup> 05 <sup>s</sup> .793213(10)
Declination, $\delta$ (J2000)	03° 27′ 19″.21053(6)	03° 27′ 19″.20911(6)
Proper Motion in $\alpha$ , $\mu_\alpha$ (mas yr <sup>-1</sup> )	-2.01(7)	-2.06(7)
Proper Motion in $\delta$ , $\mu_\delta$ (mas yr <sup>-1</sup> )	-5.20(12)	-5.21(12)
Spin Frequency, $\nu$ (Hz)	465.135245551237(10)	465.135238339217(9)
First Derivative of $\nu$ , $\dot{\nu}$ (10 <sup>-15</sup> Hz s <sup>-1</sup> )	-4.0719(2)	-4.0719(2)
Dispersion Measure, DM (cm <sup>-3</sup> pc)	297.5244(6)	297.5245(6)
First Derivative of DM (cm <sup>-3</sup> pc yr <sup>-1</sup> )	-0.0083(6)	-0.0084(6)
Orbital Period $P_b$ (days)	95.174117277(14)	95.174118753(14)
Projected Semi-Major Axis, $x$ (lt-s)	105.5934628(5)	105.5934643(5)
Eccentricity, $e$	0.436678410(3)	0.436678409(3)
Longitude of Periastron, $\omega$ (°)	141.6531042(2)	141.6524786(6)
Time of Passage through Periastron, $T_0$ (MJD)	55015.58140451(4)	55015.58158859(4)
Derivative of $x$ , $\dot{x}_o$ (10 <sup>-15</sup> lt-s s <sup>-1</sup> )	+20(3)	+21(3)
Apsidal Motion, $\dot{\omega}_o$ (° yr <sup>-1</sup> )	0.0002400(2)	0.0002400(2)
“Range” Parameter of the Shapiro Delay, $r/T_\odot$ ( $M_\odot$ )	-	1.03(3)
“Shape” Parameter of the Shapiro Delay, $s$	-	0.9760(15)
Orthometric Amplitude of the Shapiro Delay, $h_3$ ( $\mu$ s)	2.602(25)	-
Orthometric Ratio of the Shapiro Delay, $\varsigma$	0.803(6)	-
<b>Limits</b> (not fitted with other timing parameters)		
Second Derivative of $\nu$ , $\ddot{\nu}$ (10 <sup>-26</sup> Hz s <sup>-2</sup> )	4.8(1.7)	6.1(1.6)
First Derivative of $e$ , $\dot{e}$ (10 <sup>-16</sup> s <sup>-1</sup> )	1.4(6)	-
First Derivative of $P_b$ , $\dot{P}_b$ (10 <sup>-12</sup> ss <sup>-1</sup> )	-53(33)	-64(31)
<b>Derived Parameters</b>		
Spin Period, $P$ (ms)	2.14991236434921(7)	
First Derivative of Spin Period, $\dot{P}$ (10 <sup>-20</sup> ss <sup>-1</sup> )	1.88203(11)	
Characteristic Age, $\tau_c$ (10 <sup>9</sup> yr)	1.9	
Dipolar Magnetic Flux Density at the Poles, $B_0$ (10 <sup>8</sup> G)	2.0	
Galactic Longitude, $l$	37° 3363	
Galactic Latitude, $b$	-1° 0136	
Distance, $D$ (kpc)	6.4 ± 1.0	
Total Proper Motion, $\mu$ (mas yr <sup>-1</sup> )	5.60(11)	
Galactic Position Angle of Proper Motion, $\Theta_\mu$	263.9 ± 0.8°	
<b>Velocities, Solar System Barycentre Reference Frame</b>		
Transverse velocity, $V_T$ (km s <sup>-1</sup> )	168 ± 24	
Radial velocity, $\gamma$ (km s <sup>-1</sup> )	42.0 ± 4.4	
Total 3-D velocity, $V$ (km s <sup>-1</sup> )	174 ± 25	
<b>Velocities, Galactocentric Reference Frame (cylindrical)</b>		
$V_\rho$ (km s <sup>-1</sup> )	17 ± 13	
$V_\phi$ (km s <sup>-1</sup> )	-189 ± 5	
$V_z$ (km s <sup>-1</sup> )	-11 ± 4	
Total 3-D velocity, $V$ (km s <sup>-1</sup> )	190 ± 5	
<b>Velocities, Relative to Pulsar Standard of Rest (cylindrical)</b>		
$V_\phi$ (km s <sup>-1</sup> )	28 ± 5	
Total 3-D velocity, $V$ (km s <sup>-1</sup> )	37 ± 9	
<b>Derived Masses and Orbital Orientation</b>		
Mass Function, $f$ ( $M_\odot$ )	0.139558441(2)	
Orbital Inclination, $i$ (°)	77.47(15) or 102.53(15)	
Total Mass of Binary, $M_t$ ( $M_\odot$ )	2.697(29) <sup>b</sup>	
Companion Mass, $m_c$ ( $M_\odot$ )	1.029(8) <sup>b</sup>	
Pulsar Mass, $m_p$ ( $M_\odot$ )	1.667(21) <sup>b</sup>	

**Table 1.** Timing and derived parameters for PSR J1903+0327 using TEMPO and TEMPO2 as described in the text. All parameters are as measured at the Solar System Barycentre. In parentheses we present the 1- $\sigma$  uncertainties, except in a few cases (<sup>b</sup>) where we present 99.7% confidence limits.

**Table 2.** The celestial position,  $JHK_s$  magnitudes and averaged radial velocities (relative to the solar system barycentre) at both epochs of the four stars located on the slit. The position and magnitudes are obtained from the data described in Champion et al. (2008).

ID	$\alpha_{J2000}$	$\delta_{J2000}$	$J$	$H$	$K_s$	$V_1$ (km s $^{-1}$ )	$V_2$ (km s $^{-1}$ )
A	19 <sup>h</sup> 03 <sup>m</sup> 05 <sup>s</sup> .751	+03°27′21″.31	14.85 ± 0.09	14.44 ± 0.10	14.23 ± 0.19	42.0 ± 0.2	56.3 ± 0.2
B	19 <sup>h</sup> 03 <sup>m</sup> 05 <sup>s</sup> .703	+03°27′23″.83	19.49 ± 0.09	18.52 ± 0.10	18.08 ± 0.09	49.6 ± 6.1	48.6 ± 2.7
C	19 <sup>h</sup> 03 <sup>m</sup> 05 <sup>s</sup> .106	+03°27′47″.50	15.07 ± 0.09	14.52 ± 0.10	14.27 ± 0.09	45.9 ± 0.2	54.3 ± 0.4
PSR	19 <sup>h</sup> 03 <sup>m</sup> 05 <sup>s</sup> .803	+03°27′19″.18	19.22 ± 0.09	18.41 ± 0.10	18.03 ± 0.09	92.4 ± 8.3	20.2 ± 5.2

20.2 ± 5.2 km s $^{-1}$  during the second. The velocity difference between the two epochs of  $V_1 - V_2 = 72.2 \pm 9.8$  km s $^{-1}$  deviates from constant velocity at the  $7.4\sigma$  level. Between the two epochs, the averaged radial velocities of stars A and C differ by  $V_1 - V_2 = -14.2 \pm 0.3$  km s $^{-1}$  for star A and  $-8.4 \pm 0.4$  km s $^{-1}$  for star C. These differences are caused by slight differences in centring of the source on the slit Bassa et al. (2006). Based on the location of star A with respect to the centre of the slit before and after each exposure, we estimate an average offset in radial velocity of about  $-8.6 \pm 3.4$  km s $^{-1}$  for the first epoch and  $3.7 \pm 2.9$  km s $^{-1}$  for the second epoch. This is comparable to the weighted average in  $V_1 - V_2 = -12.1 \pm 0.3$  km s $^{-1}$  for stars A and C.

Subtracting these radial velocity offsets from the measured velocities of the counterpart, we obtain  $V_1 = 101.0 \pm 8.7$  km s $^{-1}$  and  $V_2 = 16.5 \pm 5.9$  km s $^{-1}$ , and a velocity difference of  $V_1 - V_2 = 85 \pm 11$  km s $^{-1}$ . This is consistent with the  $V_1 - V_2 = 88.72$  km s $^{-1}$  difference in radial velocity predicted from the pulsar timing ephemeris. This confirms that the optical counterpart to PSR J1903+0327 is the object in the 95-day orbit around the pulsar. Fig. 5 shows the radial velocity measurements of the companion and the radial velocity predictions based on the orbital parameters determined from pulsar timing. This provides an independent estimate of the mass ratio ( $R = 1.55 \pm 0.20$ ) and the systemic radial velocity of the binary,  $\gamma = 44.3 \pm 4.9$  km s $^{-1}$ , which cannot be derived from the radio timing.

### 3.3 Shapiro delay

Since the companion is a non-degenerate star, it could in principle have a strong stellar wind, which should be detectable as a variation of DM as a function of orbital phase. Such a signal would produce a distortion in our measurement of the Shapiro delay. In Fig. 6 we display the DM averaged over 36 bins of the pulsar’s mean anomaly, after correction of the long-term DM variations. For some of these intervals we have smaller amounts of data or a small range of frequencies. If these result in DM determinations with uncertainties greater than  $0.01$  cm $^{-3}$  pc, they are not depicted. We detect no DM variations greater than  $0.001$  cm $^{-3}$  pc. This means that the mass estimates derived from the Shapiro delay are accurate, within their uncertainties.

The better timing precision, larger number of TOAs, longer data span and optimised orbital coverage of our new dataset not only improve previous measurements of relativistic effects (namely the observed apsidal motion  $\dot{\omega}_o$  and the  $s$  parameter of the Shapiro delay, see Champion et al. 2008) but also allow a precise measurement of the  $r$  parameter of the Shapiro delay, in addition to a measurement of the proper motion  $\mu$  and the variation it causes on the ap-

parent size of the orbit  $\dot{x}$  (see Table 1). We now discuss the relevance of these parameters.

#### 3.3.1 Shapiro delay and component masses

With the previously available timing data it was not possible to measure the companion mass  $m_c$  from the Shapiro delay alone. The precise (and frequent) Arecibo timing has completely changed this situation, providing a very clear Shapiro delay signal (see Fig. 7). Assuming that general relativity (GR) is the correct theory of gravity, we obtain

$$\frac{m_c}{M_\odot} = \frac{r}{T_\odot} \equiv \frac{h_3}{T_\odot \varsigma^3} = 1.03 \pm 0.03, \quad (1)$$

where  $T_\odot = GM_\odot/c^3 = 4.925490947 \mu\text{s}$  is the solar mass  $M_\odot$  in time units. As usual  $G$  is Newton’s gravitational constant and  $c$  is the velocity of light. The orbital inclination derived from  $\varsigma$  is  $i = (77.4 \pm 0.4)^\circ$  or  $(102.6 \pm 0.4)^\circ$ . Given the mass function  $f$ , these values imply a pulsar mass  $m_p = (1.67 \pm 0.08)M_\odot$ , a total binary mass  $M_t = (2.70 \pm 0.11)M_\odot$  and a mass ratio  $R_s = 1.62 \pm 0.03$ .

#### 3.3.2 Estimating the uncertainties

The uncertainties quoted above were estimated using the Bayesian technique described by Splaver et al. (2002). We assume that  $m_c$  and  $\cos i$  have constant *a priori* probability. For each point in a grid of  $m_c$ ,  $\cos i$  values we calculate (trivially) the  $r$  and  $s$  parameters to describe the Shapiro delay, assuming that general relativity is the correct theory of gravitation.

We then fit a timing solution similar to that of Table 1 to the TOAs but keep  $(r, s)$  fixed. We record the resultant  $\chi^2$  and calculate the probability density for that  $(m_c, \cos i)$  space using

$$p(m_c, \cos i) = \exp \left( -\frac{\chi^2(m_c, \cos i) - \chi_{\min}^2}{2} \right), \quad (2)$$

where  $\chi_{\min}^2$  is the minimum value of  $\chi^2$  in the whole map. The contour levels that include the 68.3, 95.4 and 99.7% of all probability are displayed in Fig. 8 as the thin contours. We then project the 2-D probability density function (PDF) into the  $m_c$  and  $\cos i$  axes to calculate lateralised 1-D PDFs.

We translate the 2-D PDF of the  $(\cos i, m_c)$  space to a 2-D PDF of the  $(m_p, m_c)$  space using the mass function  $f$  Lorimer & Kramer (2005). This is then lateralised onto the  $m_p$  axis, resulting in a 1-D PDF for the pulsar mass. It is from the 1-D PDFs that we derive the uncertainties for  $\cos i$ ,  $m_p$  and  $m_c$ .

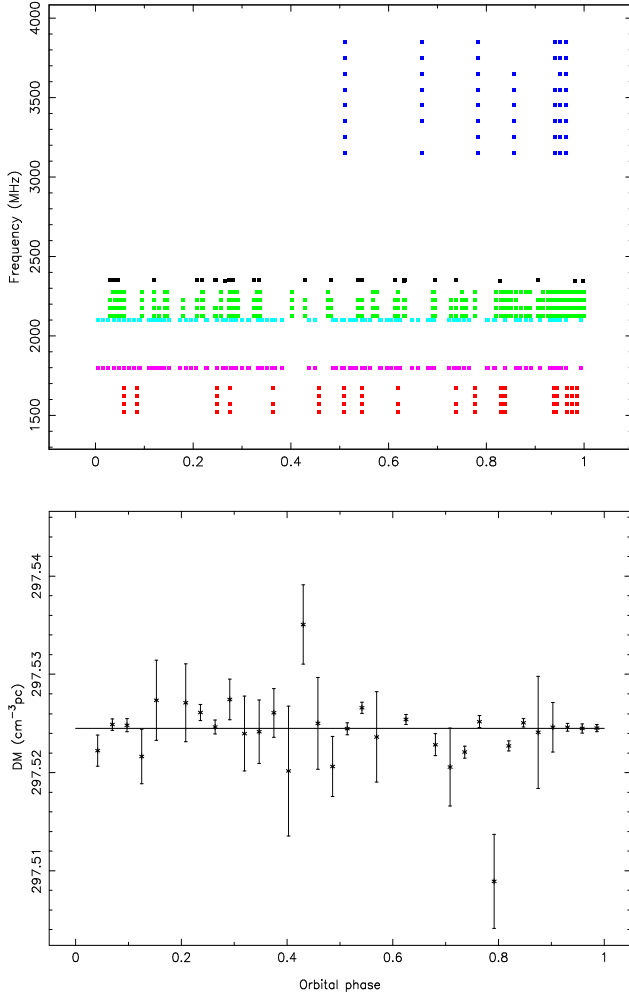


**Figure 6.** *Top:* Radio frequency of TOAs as a function of orbital phase. The orbital phases with the larger number and frequency spread of observations are those for which the DM measurements should be better. These are best at an orbital phase of 0.95, where superior conjunction happens. *Bottom:* DM as a function of orbital phase. All TOAs were divided in  $10^\circ$  orbital phase bins and a DM was derived for them, keeping all other parameters fixed.

### 3.4 Orientation of the orbit and component masses

#### 3.4.1 Kinematic effects: orbital orientation

The additional, previously undetermined parameters in Table 1 are the proper motion (with total magnitude  $\mu$  and position angle  $\Theta_\mu$ ) and the apparent variation of the size of the orbit,  $\dot{x}_o$ ; this is given by

$$\frac{\dot{x}_o}{x} = -\mu \cot i \sin(\Theta_\mu - \Omega) + \frac{\mu^2 D + a_l}{c} + \frac{\dot{x}_s}{x} + \frac{\dot{a}}{a}, \quad (3)$$

where  $i$  is the orbital inclination,  $\Omega$  is the position angle of the line of nodes,  $\dot{x}_s$  is the variation of  $x$  due to an intrinsic variation of  $i$ ,  $\dot{a}$  is a variation of the semi-major axis  $a$ ,  $D$  is the distance to the pulsar and  $a_l$  is the difference of Galactic accelerations of the binary and the solar system, projected along the line of sight.

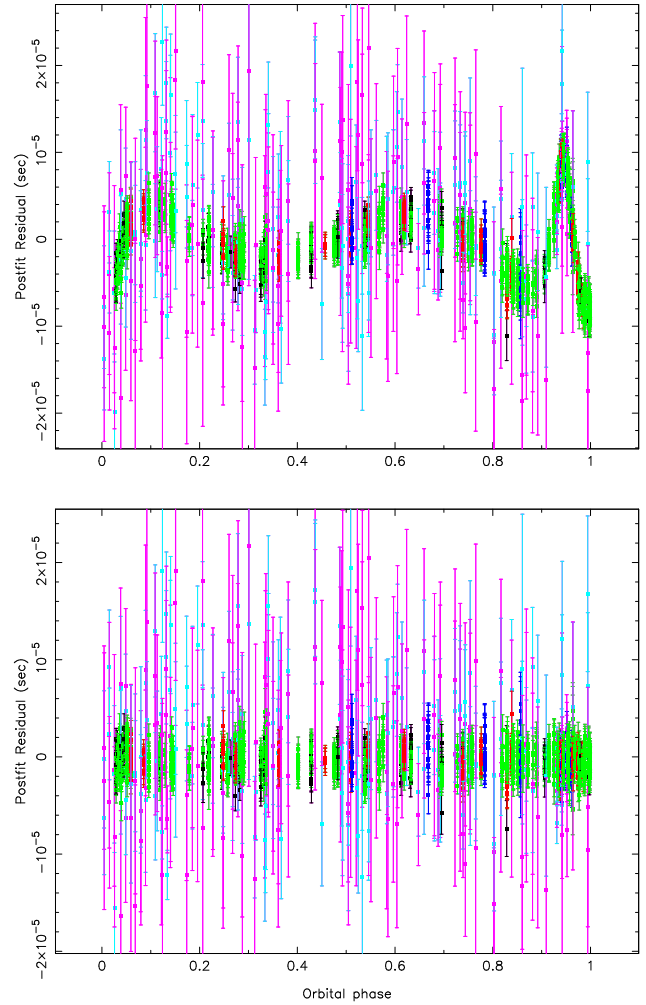


**Figure 7.** *Top:* Post-fit TOAs versus orbital phase. The Shapiro delay was not taken into account, but all Keplerian parameters were fit. *Bottom:* Post-fit TOAs versus orbital phase, with Shapiro delay taken into account. The different colours indicate different observing systems, as in Fig. 3.

The first term is by far the largest; it is an effect of the proper motion, which constantly changes the viewing geometry. If this causes a change of  $i$  as viewed from Earth then there will be a secular change of the projected size of the orbit,  $x = a \sin i/c$  Arzoumanian et al. (1996); Kopeikin (1996).

The second term describes the changing Doppler shift of the binary relative to the Solar System barycentre. For a nominal DM distance of 6.4 kpc, this amounts to  $-4.6 \times 10^{-20} \text{s}^{-1}$ . This is three orders of magnitude smaller than the measurement error; this term is thus ignored in the following discussion. The third term is due to any real changes in the orbital plane of the binary system. The only likely contribution to this is from spin-orbit coupling Smarr & Blandford (1976); Lai et al. (1995); the resulting  $\dot{x}_s$  should be one order of magnitude smaller than the measurement error (see detailed discussion in § 3.4.4). Finally, the fourth term is due to a real change in the size of the orbit. The prediction for  $\dot{a}/a$  caused by gravitational wave emission is of the order of



$10^{-26}\text{s}^{-1}$ ; many orders of magnitude too small. Therefore, only the first term is likely to give a significant contribution to the observed  $\dot{x}$ .

In this case, for each of the two possible values of  $i$  discussed above there are two possible  $(\Theta_\mu - \Omega)$  solutions; these are depicted in Fig. 9 by the intersection of the  $\dot{x}$  and  $\zeta$  lines. However, because of the uncertainty in the measurements of  $\dot{x}$  and  $\zeta$ , these two pairs of solutions merge into two wide areas centred at  $(\Theta_\mu - \Omega) \sim 90^\circ$  for  $i \sim 102.6^\circ$  and  $(\Theta_\mu - \Omega) \sim 270^\circ$  for  $i \sim 77.4^\circ$ .

### 3.4.2 Kinematic effects: apsidal motion and masses

The observed apsidal motion  $\dot{\omega}_o = (86.38 \pm 0.08)''/\text{century}$  is, in principle, a combination of the relativistic apsidal advance  $\dot{\omega}_r$ ; a kinematic contribution  $\dot{\omega}_k$  due to the changing viewing geometry of the system; and a contribution caused by spin-orbit coupling  $\dot{\omega}_s$ :

$$\dot{\omega}_o = \dot{\omega}_k + \dot{\omega}_r + \dot{\omega}_s. \quad (4)$$

We will now consider each of these terms in detail.

The  $\dot{\omega}_k$  is caused by the change of viewing geometry due to the proper motion  $\mu$  Kopeikin (1996):

$$\dot{\omega}_k = \mu' \cos(\Theta_\mu - \Omega), \quad (5)$$

where  $\mu' = \mu/\sin i = 0''.56/\text{century}$ . Given the aforementioned uncertainty of  $\Theta_\mu - \Omega$  it is impossible at the moment to know the exact value of  $\dot{\omega}_k$ , but it has a very sharp upper limit given by  $|\cos(\Theta_\mu - \Omega)| \leq 1$ . This means that uncertainty in  $\dot{\omega}_r$  caused by the lack of precise knowledge of  $\dot{\omega}_k$  is at most equal to  $\pm\mu' = 0''.56/\text{century}$ . This is more than six times larger than the current uncertainty in the measurement of  $\dot{\omega}_o$ .

This affects the precision of our estimate of the total mass of the system. If  $\dot{\omega}_r = \dot{\omega}_o$ , then the total system mass could be determined directly using

$$\dot{\omega}_r = 3n_b^{5/3} \frac{(T_\odot M_t)^{2/3}}{1 - e^2}, \quad (6)$$

where  $n_b = 2\pi/P_b$  is the orbital frequency and  $P_b$  is the orbital period (e.g. Lorimer & Kramer, 2005); the result would be  $M_t = (2.697 \pm 0.004)M_\odot$ . Because of the uncertainty of  $\dot{\omega}_k$  and  $\dot{\omega}_r = \dot{\omega}_o - \dot{\omega}_k$ , we obtain instead  $M_t = (2.697 \pm 0.029)M_\odot$  (99.7% confidence limit, see § 3.4.5).

### 3.4.3 Further uncertainty estimates

To estimate these uncertainties rigorously, we have made a second  $\chi^2$  map that uses the same principles described above, but includes a third dimension, the difference in the position angles of the proper motion and line of nodes  $\Theta_\mu - \Omega$ . This map makes use of the extra information provided by the measurements of  $\dot{x}$  and  $\dot{\omega}$ .

As before, from the values of  $m_c$  and  $\cos i$  at each point we calculate  $r$  and  $s$ . But now we also use the mass function  $f$  to calculate  $m_p$ . From the total mass  $M_t = m_p + m_c$  we calculate  $\dot{\omega}_r$  using eq. 6. From the values of  $\cos i$  and  $(\Theta_\mu - \Omega)$  at each point we calculate  $\dot{x}$  using eq. 3 and  $\dot{\omega}_k$  using eq. 5. This is made using only the best value for the proper motion  $\mu$ , which has a relatively small uncertainty.

We then fit the resulting timing solution to the TOAs,

but keep the four computed parameters fixed ( $r$ ,  $s$ ,  $\dot{x}$  and  $\dot{\omega} = \dot{\omega}_r + \dot{\omega}_k$ ). We record the resultant  $\chi^2$  and calculate the probability density for that point of the  $(m_c, \cos i, \Theta_\mu - \Omega)$  space using an expression similar to eq. 2. This 3-D “cube” of probability density is then projected onto its faces: the  $(\cos i, m_c)$  space (see thick contours in Fig. 8) and the  $(\cos i, \Theta_\mu - \Omega)$  and  $(m_c, \Theta_\mu - \Omega)$  spaces (Fig. 9). We then project this 3-D PDF onto the three axes, calculating lateralised 1-D PDFs for  $m_c$ ,  $\cos i$  and  $\Theta_\mu - \Omega$ . It is from these that we derive the uncertainties of these parameters.

In the  $(m_c, \Theta_\mu - \Omega)$  panel of Fig. 9 we can see that if  $\Theta_\mu - \Omega$  were more precisely known, we would have a much better estimate of  $m_c$ . This is the graphical demonstration that the kinematic effects are now the main source of uncertainty in the measurement of  $m_c$  and  $m_p$ , not the uncertainty intrinsic to the measurement of  $\dot{\omega}$ . We can also see that as the precision of  $\dot{x}$  improves, we will have a total of four possible values for  $\Theta_\mu - \Omega$ , two for each possibility of  $\cos i$ . The two solutions closer to the centre of Fig. 9 ( $\Theta_\mu - \Omega = 180^\circ$ ) will have a large value of  $m_c$  (and  $m_p$ ), since, according to eq. 5, for this orbital orientation  $\dot{\omega}_k < 0$ , therefore  $\dot{\omega}_r > \dot{\omega}_o$ . The opposite will be true for the two solutions closer to  $\Theta_\mu - \Omega = 0^\circ$ . Unless we can independently determine  $\cos i$  or  $\Theta_\mu - \Omega$ , we will have two degenerate values for  $m_c$  and  $m_p$ . In principle, this degeneracy can be lifted if we can measure the orbital annual parallax. This should be possible with a fourfold improvement in timing precision.

### 3.4.4 Contribution from spin-orbit coupling

Thus far we have assumed that the spin-orbit contributions to  $\dot{\omega}$  and  $\dot{x}$  are negligible. Comparing eq. 7.54 and following in Will (1993) with the more general equation in Wex (1998) we find for  $\dot{\omega}_s$ :

$$\dot{\omega}_s = 3\pi J_2 \frac{R_c^2}{P_b a^2 (1 - e^2)^2} \left( 1 - \frac{3}{2} \sin^2 \theta + \cot i \sin \theta \cos \theta \cos \Phi_0 \right), \quad (7)$$

where  $a$  is the semi-major axis of the orbit of the companion as seen from the pulsar,  $R_c$  is the companion radius (which we assume to be one solar radius),  $P_b$  and  $e$  are as listed in Table 1,  $J_2$  is the quadrupolar moment of the star,  $\theta$  is the angle between the orbital and companion’s angular momentum and  $\Phi_0$  is the longitude of the ascending node in a reference frame defined by the total angular momentum vector. For PSR J1903+0327, we obtain a maximum value of  $\dot{\omega}_s = J_2 \times 7.9 \times 10^5 ''/\text{century}$ .

As we have shown in § 3.1, the companion star has a mass, age and temperature similar to that of the Sun. Such stars should rotate slowly like the Sun Irwin et al. (2009); the latter has a rotational velocity of  $v_{\text{rot},\odot} = 2 \text{ km s}^{-1}$ . This should result in a quadrupolar moment similar to that of the Sun,  $J_{2,\odot} \sim 1.7 \times 10^{-7}$ . For this value of  $J_2$  we get  $\dot{\omega}_s \sim 0''.013/\text{century}$ , about seven times smaller than the measurement uncertainty of  $\dot{\omega}_o$ .

However, because the companion’s rotation is not well constrained by the optical measurements (which indicate  $v_{\text{rot}} \sin i_* < 140 \text{ km s}^{-1}$ , 3- $\sigma$ , see § 2.1), we can use the agreement between  $h_3$ ,  $\zeta$  and  $\dot{\omega}_r$  to constrain  $\dot{\omega}_s$  assuming that GR is the correct theory of gravity. The minimum total mass compatible (at the 1- $\sigma$  level) with  $h_3$  and  $\zeta$  is  $2.59M_\odot$ . The corresponding minimum  $\dot{\omega}_r$  ( $84.1''/\text{century}$ ) can then be used to derive a 1- $\sigma$  limit of  $\dot{\omega}_s = \dot{\omega}_o - \dot{\omega}_{r,\text{min}} < 2.3''/\text{century}$

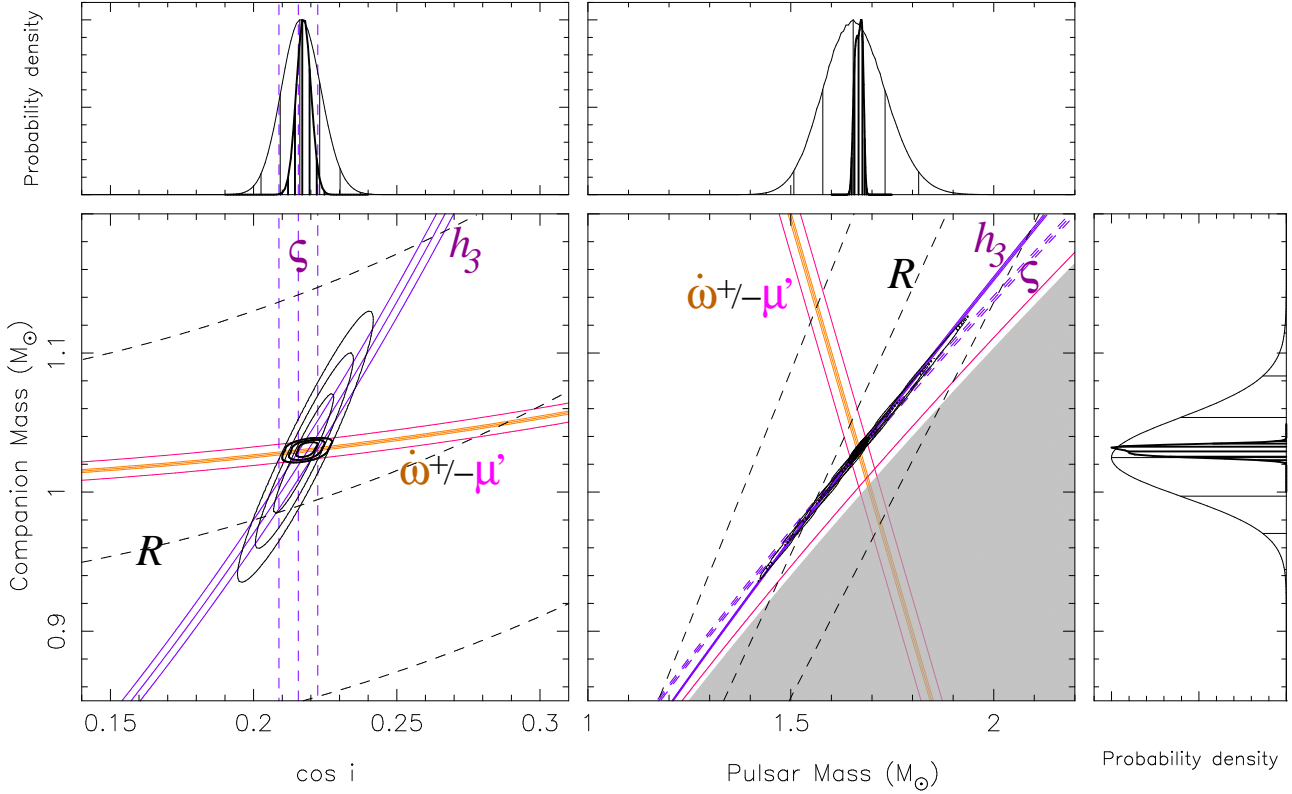


**Figure 8.** Companion mass as a function of  $\cos i$  and  $m_p$ . The thick contour levels are derived from a 3-D  $\chi^2$  map of the  $\cos i$ ,  $m_c$  and  $\Omega$  space (where  $\Omega$  is the position angle of the line of nodes) and then collapsed on the planes represented in the figure (see text for details). The thin contour levels represent a 2-D  $\chi^2$  map of the  $\cos i - m_c$  space calculated taking only the Shapiro delay into account. The lines represent the constraints derived from the spectroscopic mass ratio ( $R$ , black dashed), the apsidal motion ( $\dot{\omega}$ , solid orange - here with increased uncertainty due to the proper motion, solid pink), the harmonic amplitude ( $h_3$ ) and harmonic ratio ( $\zeta$ ) of the Shapiro delay (in purple) and finally an upper limit on the inclination given by  $\dot{x}$  (pink solid line). The gray area in the mass-mass diagram is excluded by  $\sin i \leq 1$ . In the marginal plots we can see that the 1-D probability distribution functions for the pulsar and companion masses are much narrower when the apsidal motion (even with uncertainty caused by the proper motion) is taken into account (thick lines), but this assumes that there are no significant classical contributions to  $\dot{\omega}$ . The latter must be  $< 2.3''/\text{century}$  ( $1-\sigma$ ) given the agreement between the  $h_3$ ,  $\zeta$  and  $\dot{\omega} \pm \mu'$  bands.

(here we are assuming a median expected value of 0 for  $\dot{\omega}_k$ ). Future optical/near infrared measurements might be able to better constrain  $v_{\text{rot}}$ . If this is small then the agreement of the 3 different PK parameters can be used directly as a test of general relativity.

To calculate  $\dot{x}_s$ , we use eq. 81 of Wex (1998) to derive

$$\frac{\dot{x}_s}{x} = 3\pi J_2 \frac{R_c^2}{P_b a^2 (1 - e^2)^2} \cot i \cos \theta \sin \theta \sin \Phi_0. \quad (8)$$

Using the parameters above, we obtain  $|\dot{x}_s/x| < 2.2 \times 10^{-18} \text{ s}^{-1}$ , which is one order of magnitude below the measurement error. Therefore, an improved measurement of  $\dot{x}$  will likely improve the determination of the orbital orientation.

#### 3.4.5 Component masses and orbital inclination

From the 3-D map, we obtain the following parameters:  $i = (77.47 \pm 0.15)^\circ$  or  $(102.53 \pm 0.15)^\circ$  ( $1-\sigma$ ),  $M_t = (2.697 \pm 0.029) M_\odot$ ,  $m_c = (1.029 \pm 0.008) M_\odot$ ,  $m_p = (1.667 \pm 0.021) M_\odot$  and  $R = 1.620 \pm 0.008$ . The underlying probability distribution functions for these parameters have a shape that is very different from a Gaussian curve (see

Fig. 8), therefore it is not very meaningful to refer to  $\sigma$  limits. For all the previous values we indicated instead 99.7% confidence limits. These values and their uncertainties can be understood qualitatively as the result of the intersection of the  $1-\sigma$  bands of  $h_3$  and  $\dot{\omega}_r$ . Their intersection results in measurement of  $i$  that is more precise than the value derived from  $s$  (or  $\zeta$ ). Such a result cannot be understood using the regular  $r, s$  parameterization of the Shapiro delay.

These values are entirely consistent with those derived solely from the Shapiro delay in § 3.3, but much more precise, despite the uncertainty introduced by  $\dot{\omega}_k$ .

## 4 IMPLICATIONS

### 4.1 Neutron star mass

The recent mass measurement of PSR J1614–2230 ( $m_p = (1.97 \pm 0.4) M_\odot$ ,  $1-\sigma$ , see Demorest et al. 2010) rules out the presence of hyperons, bosons and free quarks at densities comparable to the nuclear saturation density, and demonstrates that NSs can be stable at masses well above the Chandrasekhar mass. The mass measurement of PSR J1903+0327 ( $m_p = (1.667 \pm 0.021) M_\odot$ , see § 3.4)

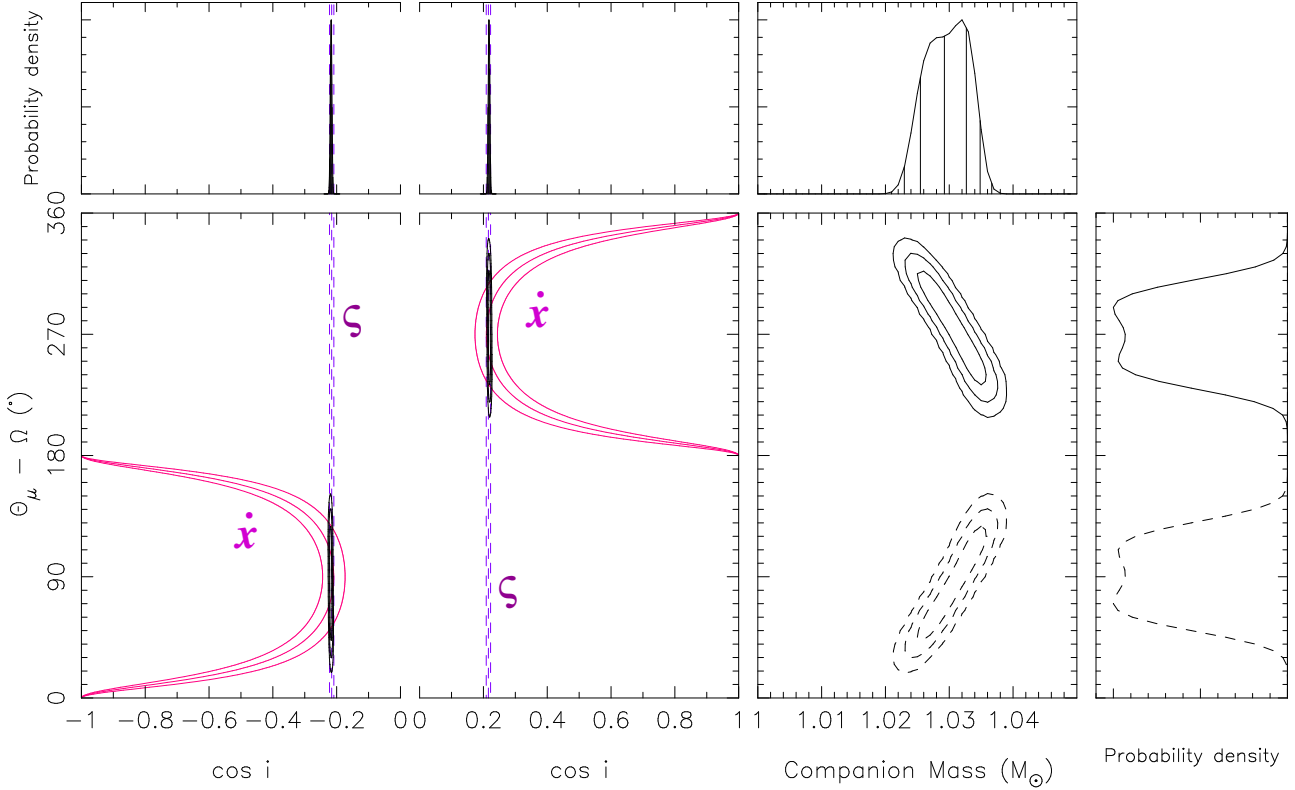


**Figure 9.** Confidence contours for  $\cos i$  and  $m_c$  as a function of the orientation of the line of nodes relative to the direction of the proper motion  $\Theta_\mu - \Omega$ . The contour levels include 66.3, 95.4 and 99.7% of the total probability, which is derived from a 3-D  $\chi^2$  map of the  $(\cos i, m_c, \Theta_\mu - \Omega)$  space and then collapsed onto the planes represented in the figure. The dashed contour lines indicate  $90^\circ < i < 180^\circ$ . The vertical purple dashed lines are the constraints introduced by the harmonic ratio of the Shapiro delay ( $\zeta$ ), the pink solid curves are the constraints derived from the measurement of  $\dot{x}$ . In the marginal plots are displayed the 1-D probability distribution functions. We can see that there is still a large uncertainty in  $(\Theta_\mu - \Omega)$ . This introduces a large uncertainty in the mass estimates (of which  $m_c$  is shown in the plot).

supports the latter conclusion, being also inconsistent with the softest proposed equations of state for super-dense matter. This plus the mass measurements of PSR J0437–4715 Verbiest et al. (2008) and PSR J0621+1002 Splaver et al. (2002) confirm beyond doubt the results of a previous statistical analysis of masses of several binary MSPs in globular clusters Freire et al. (2008a), which showed that MSPs have a much wider mass distribution than observed among the members of double neutron star systems. The likely cause is the accretion episode that spun up these NSs Bhattacharya & van den Heuvel (1991); Lorimer (2008).

There are several reasons why PSR J1903+0327 appears to be a normal MSP (i.e., spun up by accretion of mass from a companion): a) its spin period is typical of that of MSPs and  $\sim 8$  times shorter than that of the fastest young pulsar, PSR J0537–6910, near the N157B supernova remnant in the Large Magellanic Cloud Marshall et al. (1998) b) its magnetic field ( $B_0$ ) is similar to those observed among MSPs and two orders of magnitude smaller than the smallest  $B_0$  thus far observed for a young pulsar,  $3 \times 10^{10}$  G for PSR J1852+0040, a 105-ms X-ray pulsar near the centre of the supernova remnant Kesteven 79 Halpern & Gotthelf (2010) c) its mass suggests it accreted mass from a former donor star. Precise mass measurements for components of double neutron star systems range from  $1.25 M_\odot$  Kramer et al. (2006) to  $1.44 M_\odot$  Weisberg et al. (2010); this

shows that a large majority of NSs form with masses near the Chandrasekhar limit Lorimer (2008). If this was also the case for PSR J1903+0327 then it must have gained  $\Delta M \sim 0.22 - 0.42 M_\odot$  during accretion, which is well within the range expected for low-mass and intermediate-mass binary pulsars (Pfahl et al. 2002). All of this is inconsistent with scenarios where PSR J1903+0327 forms directly from the collapse of a single star. Even alternative MSP formation scenarios (like merger of massive WDs or accretion induced collapse) require two stars to form the MSP.

#### 4.2 PSR J1903+0327 is not a triple system

The discovery that the companion to PSR J1903+0327 is the MS star previously suspected of being associated with the system immediately rules out the detailed triple system scenario proposed in Champion et al. (2008). Our measurement of the variation of eccentricity had already ruled out the possibility that the Kozai mechanism is the origin of the observed eccentricity (Gopakumar, Bagchi & Ray 2009).

Despite this, it is clear that the present companion cannot be the star that recycled the pulsar. If it were, then it must have at some point filled the region where matter will remain bound to it (its “Roche lobe”) in order to transfer matter to the companion. The problem is that at the closest approach between the stars the companion is  $\sim 23$  times

smaller than its present Roche lobe. Being an unevolved MS star it was even smaller in the past<sup>3</sup> and even less likely to have supplied the material that recycled this pulsar.

Could the former donor have exchanged orbits with the main-sequence companion and now orbit the J1903+0327 binary system at a large distance? If there were a third component in the system, the J1903+0327 binary system would be accelerating towards it, with a line-of-sight component given by  $a_l$ . This should produce a variation of its orbital period given by  $\dot{P}_b/P_b = a_l/c$ . Variations of  $a_l$  due to the relative motion of the J1903+0327 binary system and the outer component should produce a variation of the first derivative of the spin frequency ( $\dot{\nu}$ ),  $\ddot{\nu}$  (e.g., Backer, Foster & Sallmen, 1993). Our measurements of  $\dot{P}_b$  and  $\ddot{\nu}$  are not statistically significant (see Table 1), i.e., we detect no third component in this system. If the former donor still exists, it is no longer bound to this system.

### 4.3 Motion of PSR J1903+0327 in the Galaxy

A possible explanation for the absence of the former donor is that it might have been exchanged by the present companion. Before the discovery of PSR J1903+0327, this was the only mechanism known to produce MSP binaries with eccentric orbits. This can only occur in environments with high stellar densities such as the cores of globular clusters Phinney (1992) or, hypothetically, the Galactic Centre. This is the reason why all other eccentric binary MSPs are observed in globular clusters Ransom et al. (2004); Freire et al. (2004); Ransom et al. (2005); Freire et al. (2008b). For this reason it was proposed in Champion et al. (2008) that PSR J1903+0327 might have formed in such an environment and subsequently have been ejected by the recoil produced by the presumed exchange interaction.

To investigate this possibility, we used the radial velocity  $\gamma$  and the pulsar's Galactic coordinates, DM distance, and proper motion to derive all three coordinates of its position in space and all three components of its velocity vector, as in Wex et al. (2000) and Lazaridis et al. (2009); the results are displayed in Table 1. We can thus calculate the past trajectory of the binary in the Galactic potential Kuijken & Gilmore (1989). We implement this process in a Monte Carlo simulation of 10000 orbits in the model Galactic potential. We take the uncertainties of  $\mu$ ,  $\gamma$  and distance<sup>4</sup> into account by integrating many orbits with random initial conditions having a distribution of parameters consistent with the observed values and uncertainties. We also compare our results with those obtained using an alternative model for the Galactic potential Paczyński (1990).

Our results are presented in Figs. 10 and 11. The starting orbits have a range of proper motions and systemic velocities consistent with the uncertainties in Table 1. We also assume a 1- $\sigma$  relative uncertainty of 15% in the distance. For each point we integrate the pulsar orbit back in time

for about 300 Myr and record the maximum ( $R_{\max}$ ) and minimum ( $R_{\min}$ ) distances to the centre of the Galaxy. The diagonal black line shown in the top plot of Fig. 11 indicates circular orbits and the gray line eccentricities of 0.2.  $R_{\max}$  cannot be smaller than the minimum possible distance to the Galactic centre at present (blue line), this is given by  $R_0 \sin l$ , where  $R_0$  is the Sun's distance to the Galactic centre (7.7 kpc in the model used for this simulation Kuijken & Gilmore (1989)) and  $l$  is the pulsar's Galactic longitude,  $37.33^\circ$ . In this plot we can see that the minimum possible distance from the Galactic centre is always larger than 3 kpc. This excludes formation in the Galactic centre and in the bulge globular clusters.

It is also apparent from our simulations that the distance from the Galactic plane never exceeds 270 pc (99.7% confidence limit), which is unusual for MSPs. The globular clusters observed outside the bulge have a wide distribution of Galactic heights Harris (1996), which implies that most of them orbit the Galaxy well outside the plane. The formation of PSR J1903+0327 in such a cluster would require that the system is ejected at the exact time the cluster is crossing the Galactic plane and that the resulting velocity is very nearly in the Galactic plane and close to the average local Galactic rotation (the system's current peculiar velocity is  $37 \pm 9 \text{ km s}^{-1}$ , see bottom plot of Fig. 11). We find this possibility highly unlikely. The probability of formation in an exchange interaction appears therefore to be extremely small.

## 5 FORMATION OF PSR J1903+0327

To summarise, the measured mass of PSR J1903+0327 (plus its small spin period and magnetic field) make any scenarios where it forms as it is unlikely; all pulsar characteristics are consistent with it having been recycled (§ 4.1). Our limits on the variation of the eccentricity and our optical detection exclude the triple system scenario proposed in Champion et al. (2008, § 4.2). In particular, we find that the present companion is not the donor star that recycled the pulsar; if this former donor still exists it is no longer bound to the system. Furthermore, our calculations of the 3-D systemic motion (§ 4.3) show that it is unlikely that the system originated in an environment with high stellar density. Therefore, it is unlikely that the former donor star was exchanged by the present companion. So how did PSR J1903+0327 form? And what happened to the former donor star?

### 5.1 Multiple star spiral-in

We suggest that the system started as a triple (indicated below in square brackets), where the outer companion (the present MS star companion) was initially on a much wider orbit than at present. The inner binary system (indicated in parentheses) had a much shorter orbital period and consisted of two somewhat more massive MS stars:

$$[(\text{MS} + \text{MS}; 12 + 2M_\odot; 20\text{d}) + \text{MS}; 1M_\odot; 1000\text{d}]$$

(the numbers are conjectural, we show them for illustrative purposes only). The more massive star (the progenitor of the pulsar), evolves and becomes a red supergiant (RSG):

<sup>3</sup> If this star had ever filled its Roche lobe the orbit would have been circularised. This is inconsistent with the present large and non-varying eccentricity.

<sup>4</sup> We used a 1- $\sigma$  relative uncertainty in the distance of 15% such that it is similar to the range of optically derived distances.

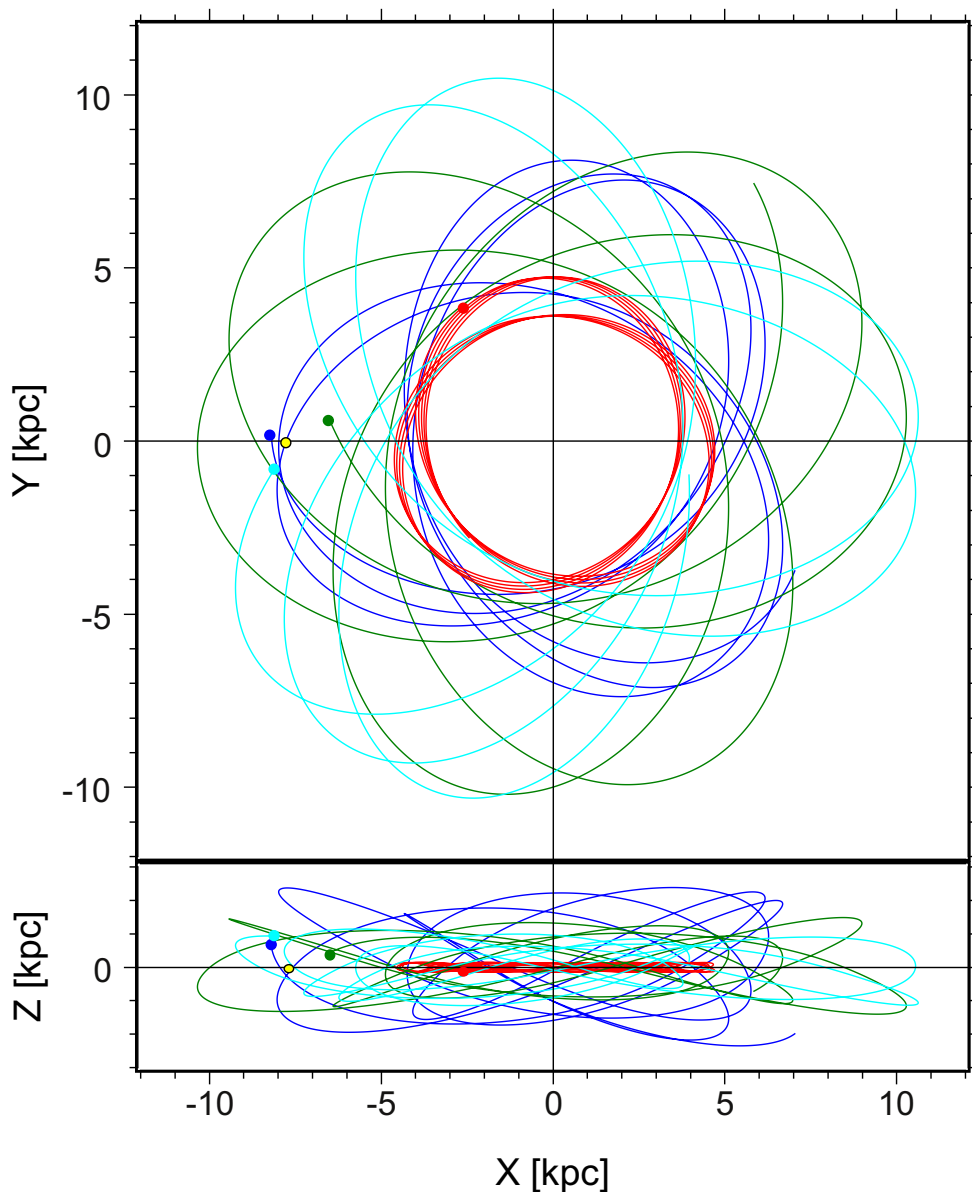


**Figure 10.** Present Galactic positions (dots) and past orbits, integrated for 1 Gyr (solid curves) of the four MSPs with known radial velocities: PSR J1903+0327 (Red), PSR J1012+5307 [Dark Blue, Lazaridis et al. (2009)], PSR J1023+0038 [Light Blue, Thorstensen & Armstrong (2005); Archibald et al. (2009)] and PSR J1738+0333 [Olive Green]. The Sun's position is indicated by the yellow circle. In the top plot we look at the Galaxy from the North Galactic pole, in the bottom plot from the direction in the Galactic plane perpendicular to the line from the Sun to the Galactic centre. We can see that PSR J1903+0327 is always near the Galactic plane, and that its orbital velocity about the Galaxy has a relatively small eccentricity.

$[(\text{RSG} + \text{MS}; 12 + 2M_{\odot}; 20\text{d}) + \text{MS}; 1M_{\odot}; 1000\text{d}]$

At this point, it starts transferring mass to the other component in the inner binary. In such a situation, mass transfer is generally unstable, and the envelope of the RSG is expected to engulf the companion and lead to a common envelope (CE) phase, where the helium core of the RSG and the inner companion are embedded in the envelope of the RSG. Because of friction with the envelope, the orbit of this

embedded binary will decay, releasing orbital energy in the process. If this energy is sufficient to eject the envelope, this will leave a much closer binary consisting of a helium star and the more-or-less unaffected inner companion (see, e.g., Bhattacharya & van den Heuvel 1991):

$[(\text{He} + \text{MS}; 3 + 2M_{\odot}; 3\text{d}) + \text{MS}; 1M_{\odot}; 1000\text{d}]$

If the outer component of the triple system is close enough, it may also be affected by this CE phase, since the en-

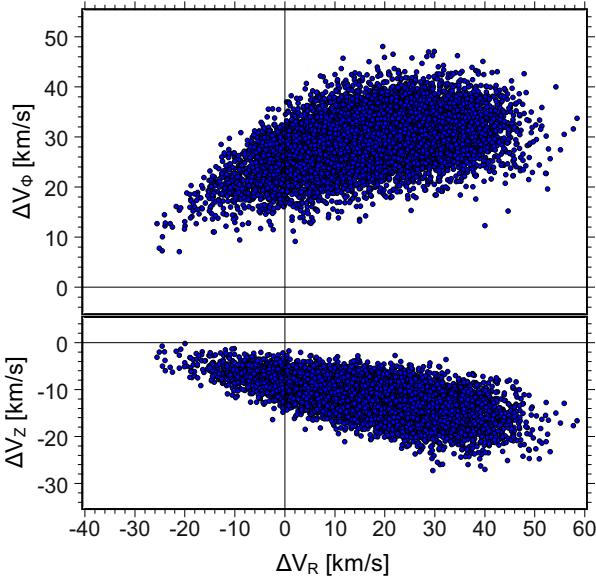
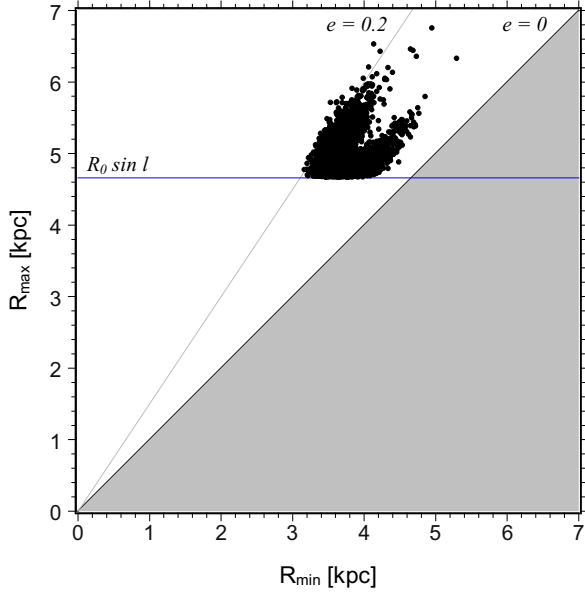


**Figure 11.** Monte-Carlo simulation of 10000 pulsar orbits. *Top:* Minimum and maximum distances from the centre of the Galaxy. We can see here that the pulsar is never within 3 kpc from the centre of the Galaxy. *Bottom:* Starting velocities in previous simulation relative to each simulated pulsar’s average of local velocities (i.e., the system’s *peculiar velocity*).

velope will greatly expand because of the orbital energy that is being deposited within it (to radii of  $\sim 5 - 10$  AU; see, e.g., Podsiadlowski 2001). It will also be engulfed by the expanding envelope and will also experience a spiral-in phase Eggleton & Verbunt (1986). This will produce a much closer triple system. Without realistic hydrodynamical simulations, it is difficult to determine the post-CE parameters. Here, we will consider two potential outcomes, which we will discuss in more detail later:

a) [(He + MS; 3 +  $2M_{\odot}$ ; 2d) + MS;  $1M_{\odot}$ ; 100d]

or

b) [(He + MS; 3 +  $2M_{\odot}$ ; 0.8d) + MS;  $1M_{\odot}$ ; 50d]

Eventually, the He core will explode in a supernova and produce a NS. The sudden mass loss associated with this event will make the orbits of the other two components wider and somewhat eccentric:

a) [(NS + MS; 1.4 +  $2M_{\odot}$ ; 2.5d) + MS;  $1M_{\odot}$ ; 120d,  $e = 0.1$ ]

or

b) [(NS + MS; 1.4 +  $2M_{\odot}$ ; 8hr) + MS;  $1M_{\odot}$ ; 70d,  $e = 0.44$ ]

This event could be either a normal Fe-core collapse supernova (SN) or an electron-capture (e-capture) supernova (see Podsiadlowski et al. 2004, and further references therein). Given the fact that the system remained bound after the explosion, it is not likely that the SN produced a major kick, nor large fractional mass loss, particularly under scenario “a”, where the system is wider and acquires a small eccentricity. This is consistent with the observed peculiar velocity for the system, which is smaller than for the other systems where we can make a complete determination of this quantity (see Fig. 10). We note too that such SN characteristics are expected from e-capture supernovae.

## 5.2 Post-supernova evolution

At this stage the inner binary resembles the progenitor of a typical low- or intermediate-mass X-ray binary (L/IMXB). Once the normal stellar component of the inner binary has evolved to fill its Roche lobe, mass transfer to the NS will start to increase its mass and spin it up to millisecond periods (see, e.g., Pfahl et al. 2002). Initially, when the separation of the inner binary is sufficiently small compared to the periastron of the outer component, the evolution of the L/IMXB will not be significantly affected by the presence of the outer component.

If the mass-transfer rate is very high, mass loss from the inner binary will cause the orbit of the outer component to widen to some degree. However, even for conservative mass transfer the inner binary is generally expected to widen more drastically, in particular in the 2.5 day scenario (scenario “a” in § 5.1; see Podsiadlowski et al. 2002):

[(MSP + MS; 1.67 +  $0.3M_{\odot}$ ; 50d) + MS;  $1M_{\odot}$ ; 150d,  $e = 0.1$ ]

until its separation reaches a critical fraction of the perias-

tron distance of the outer companion. This leads to a chaotic three-body interaction (see, e.g., Hut 1984; Phillips 1993). One of the most probable outcomes is the ejection of the least massive component – in this case most likely the mass donor in the inner binary, leaving a bound, eccentric binary system consisting of the MSP and the formerly outer companion, in an orbit tighter than before:

$$(\text{MSP} + \text{MS}; 1.67 + 1\text{M}_{\odot}; 95\text{d}, e = 0.44)$$

If the starting orbital period is small ( $P_B < 8$  hr, scenario b in § 5.1), then gravitational radiation might lead to the destruction of the remnant of the former donor by the newly formed MSP, very much in the same way as PSR 1957+20, the black-widow pulsar (Fruchter et al. 1988), is evaporating its companion (although in the latter case the process might take several Hubble times). This is a possible formation channel for isolated MSPs. Since these represent  $\sim 20\%$  of the known MSPs in the Galactic disk, this should not be too unlikely a scenario. The end result would also resemble the J1903+0327 binary system.

### 5.3 Alternative scenarios

One can imagine alternative triple scenarios to the one outlined above. For example, it is possible that the progenitor of the MSP was initially the outer component of a stable triple system. When this massive star evolved to become a red supergiant, it could have engulfed the inner binary completely, leading to a spiral-in of that binary inside the common envelope. As it spirals in, its orbit could become disrupted by the tide induced by the more massive component; both of its components then start orbiting the core of the more massive He star independently, but at different distances given their different orbital velocities prior to disruption. This would produce a result quite similar to the double star spiral-in. Another possibility is that this binary survived the CE phase, but it was later disrupted when its orbital radius increases due to a mass transfer stage.

## 6 CONCLUSIONS

Our Arecibo and Green Bank radio timing observations include a full determination of the relativistic Shapiro delay, a very precise measurement of the apsidal motion and new constraints of the orbital orientation of the system. Through a detailed analysis of all of these, we derive new constraints on the masses of the pulsar and companion. The mass of the pulsar ( $1.667 \pm 0.021 \text{ M}_{\odot}$ ) adds to a growing population of NSs with masses which significantly exceed  $1.4 \text{ M}_{\odot}$  and rules out some of the proposed equations of state of superdense matter. This high mass also suggests that the pulsar was recycled.

Our observations with the Very Large Telescope reveal shifts in the spectral lines of the suspected companion to PSR J1903+0327, which show that it has the 95-day orbital motion expected for the pulsar’s binary companion. This star has characteristics very similar to the Sun; making this system unique among all known binary MSPs. A detailed discussion of the results of the radio timing and optical spectroscopy rules out most proposed formation mechanisms.

We are then forced to accept the only remaining possibility, i.e., that the system originated from a triple system with a compact inner component and the presently observed MS companion as the outer component. The inner compact binary then formed the observed MSP, with the elimination of the former donor star (i.e., evolution towards an “isolated” MSP), or its ejection from the system.

Detailed stellar evolution simulations of the formation of this system might provide new insights on how MSPs form. As an example, the mass loss and kick velocities associated with the supernova event that formed this NS must have been small enough to allow the whole system to remain bound. Such a gentle formation would produce a small recoil velocity for the whole system; this is consistent with the small peculiar velocity observed at present. This would generally favour alternative small-kick formation mechanisms, like electron capture supernovae. This means that a dynamical study of this system could lead to a conclusive demonstration of alternative formation channels for NSs in general. Some of these exotic mechanisms (for example, white dwarf mergers) could be especially important for explaining the existence of isolated MSPs.

## ACKNOWLEDGEMENTS

This work was supported by the NSF through a cooperative agreement with Cornell University to operate the Arecibo Observatory. The National Radio Astronomy Observatory is a facility of the National Science Foundation operated under cooperative agreement by Associated Universities, Inc. Pulsar research at UBC is supported by an NSERC Discovery Grant. V.M.K. receives support via an NSERC Discovery Grant, CIFAR, FQRNT, and from the Lorne Trottier Chair and a Canada Research Chair. J.W.T.H. is a Veni Fellow of The Netherlands Organisation for Scientific Research (NWO). M.A.M and D.R.L are supported by the West Virginia EPSCoR program and the Research Corporation for Scientific Advancement. J.P.W.V is supported by the European Union under Marie Curie Intra-European Fellowship 236394. D.J.N. was supported by NSF grant AST 0647820 to Bryn Mawr College. We also thank the referee, Peter P. Eggleton, for the careful review and many constructive suggestions.

## REFERENCES

- Appenzeller, I. et al. 1998, *The Messenger*, 94, 1
- Archibald, A. M. et al. 2009, *Science*, 324, 1411
- Arzoumanian, Z., Joshi, K., Rasio, F., & Thorsett, S. E. 1996, in *Pulsars: Problems and Progress*, IAU Colloquium 160, ed. S. Johnston, M. A. Walker, & M. Bailes, (San Francisco: Astronomical Society of the Pacific), 525
- Backer, D. C., Foster, R. F., & Sallmen, S. 1993, *Nature*, 365, 817
- Bassa, C. G., van Kerkwijk, M. H., Koester, D., & Verbunt, F. 2006, *A&A*, 456, 295
- Bhattacharya, D. & van den Heuvel, E. P. J. 1991, *Phys. Rep.*, 203, 1
- Cenarro, A. J., Cardiel, N., Gorgas, J., Peletier, R. F., Vazdekis, A., & Prada, F. 2001, *MNRAS*, 326, 959



- Champion, D. J. et al. 2008, *Science*, 320, 1309
- Cordes, J. M. et al. 2006, *ApJ*, 637, 446
- Cordes, J. M. & Lazio, T. J. W. 2002, astro-ph/0207156
- Damour, T. & Deruelle, N. 1985, *Ann. Inst. H. Poincaré (Physique Théorique)*, 43, 107
- Damour, T. & Deruelle, N. 1986, *Ann. Inst. H. Poincaré (Physique Théorique)*, 44, 263
- Demorest, P., Pennucci, T., Ransom, S., Roberts, M., & Hessels, J. W. T. 2010, *Nature*, 467, 1081
- Demorest, P. B. 2007. PhD thesis, University of California, Berkeley
- Dowd, A., Sisk, W., & Hagen, J. 2000, in *Pulsar Astronomy - 2000 and Beyond*, IAU Colloquium 177, ed. M. Kramer, N. Wex, & R. Wielebinski, (San Francisco: Astronomical Society of the Pacific), 275
- Eggleton, P. P. & Verbunt, F. 1986, *MNRAS*, 220, 13P
- Folkner, W. M., Williams, J. G., & Boggs, D. H. 2008. Jpl planetary and lunar ephemeris, de421. Technical Report IOM 343R-08-003, NASA Jet Propulsion Laboratory
- Freire, P. C., Gupta, Y., Ransom, S. M., & Ishwara-Chandra, C. H. 2004, *ApJ*, 606, L53
- Freire, P. C. C. & Wex, N. 2010, *MNRAS*, 409, 199
- Freire, P. C. C., Ransom, S. M., Bégin, S., Stairs, I. H., Hessels, J. W. T., Frey, L. H., & Camilo, F. 2008b, *ApJ*, 675, 670
- Freire, P. C. C., Wolszczan, A., van den Berg, M., & Hessels, J. W. T. 2008a, *ApJ*, 679, 1433
- Fruchter, A. S., Stinebring, D. R., & Taylor, J. H. 1988, *Nature*, 333, 237
- Girardi, L., Bressan, A., Bertelli, G., & Chiosi, C. 2000, *A&A*, 141, 371
- Gopakumar, A., Bagchi, M., & Ray, A. 2009, *MNRAS*, 399, L123
- Halpern, J. P. & Gotthelf, E. V. 2010, *ApJ*, 709, 436
- Harris, W. E. 1996, *AJ*, 112, 1487. Updated version at <http://www.physics.mcmaster.ca/resources/globular.html>
- Hobbs, G. B., Edwards, R. T., & Manchester, R. N. 2006, *MNRAS*, 369, 655
- Horne, K. 1986, *PASP*, 98, 609
- Hut, P. 1984, *ApJS*, 55, 301
- Hynes, R. I. 2002, *A&A*, 382, 752
- Irwin, J., Aigrain, S., Bouvier, J., Hebb, L., Hodgkin, S., Irwin, M., & Moraux, E. 2009, *MNRAS*, 392, 1456
- Kaplan, D. L. et al. 2005, *PASP*, 117, 643
- Kopeikin, S. M. 1996, *ApJ*, 467, L93
- Kozai, Y. 1962, *AJ*, 67, 591
- Kramer, M. et al. 2006, *Science*, 314, 97
- Kuijken, K. & Gilmore, G. 1989, *MNRAS*, 239, 571
- Lai, D., Bildsten, L., & Kaspi, V. M. 1995, *ApJ*, 452, 819
- Lazaridis, K. et al. 2009, *MNRAS*, 400, 805
- Lorimer, D. R. 2008, *Living Reviews in Relativity*. <http://relativity.livingreviews.org/Articles/lrr-2008-8/>
- Lorimer, D. R. and Kramer, M. 2005, *Handbook of Pulsar Astronomy*, (Cambridge: Cambridge University Press)
- Marshall, F. E., Gotthelf, E. V., Zhang, W., Middleditch, J., & Wang, Q. D. 1998, *ApJL*, 499, L179
- Moffat, A. F. J. 1969, *A&A*, 3, 455
- Munari, U., Sordo, R., Castelli, F., & Zwitter, T. 2005, *A&A*, 442, 1127
- Paczyński, B. 1990, *ApJ*, 348, 485
- Pfahl, E., Rappaport, S., & Podsiadlowski, P. 2002, *ApJ*, 573, 283
- Phillips, J. A. 1993, in *Planets Around Pulsars*, ed. J. A. Phillips, S. E. Thorsett, & S. R. Kulkarni, volume 36, Astronomical Society of the Pacific Conference Series, 321
- Phinney, E. S. 1992, *Philosophical Transactions of the Royal Society of London A*, 341, 39
- Phinney, E. S. & Kulkarni, S. R. 1994, *Ann. Rev. Astr. Ap.*, 32, 591
- Podsiadlowski, P. 2001, in *Evolution of Binary and Multiple Star Systems*, ed. P. Podsiadlowski, S. Rappaport, A. R. King, F. D'Antona, & L. Burderi, volume 229 of Astronomical Society of the Pacific Conference Series, 239
- Podsiadlowski, P., Rappaport, S., & Pfahl, E. D. 2002, *ApJ*, 565, 1107
- Podsiadlowski, P., Langer, N., Poelarends, A. J. T., Rappaport, S., Heger, A., & Pfahl, E. 2004, *ApJ*, 612, 1044
- Ransom, S. M., Hessels, J. W. T., Stairs, I. H., Freire, P. C. C., Camilo, F., Kaspi, V. M., & Kaplan, D. L. 2005, *Science*, 307, 892
- Ransom, S. M., Stairs, I. H., Backer, D. C., Greenhill, L. J., Bassa, C. G., Hessels, J. W. T., & Kaspi, V. M. 2004, *ApJ*, 604, 328
- Smarr, L. L. & Blandford, R. 1976, *ApJ*, 207, 574
- Splaver, E. M., Nice, D. J., Arzoumanian, Z., Camilo, F., Lyne, A. G., & Stairs, I. H. 2002, *ApJ*, 581, 509
- Stairs, I. H., Thorsett, S. E., & Arzoumanian, Z. 2004, *Phys. Rev. Lett.*, 93(14), 141101
- Standish, E. M. 1998, *JPL Planetary and Lunar Ephemerides*, DE405/LE405, Memo IOM 312.F-98-048, (Pasadena: JPL). <http://ssd.jpl.nasa.gov/iau-comm4/de405iom/de405iom.pdf>
- Tauris, T. M. & van den Heuvel, E. P. J. 2006, *Formation and evolution of compact stellar X-ray sources*, 623
- Taylor, J. H. 1992, *Philosophical Transactions of the Royal Society of London A*, 341, 117
- Thorstensen, J. R. & Armstrong, E. 2005, *AJ*, 130, 759
- Verbiest, J. P. W. et al. 2008, *ApJ*, 679, 675
- Weisberg, J. M., Nice, D. J., & Taylor, J. H. 2010, *ApJ*, 722, 1030
- Wex, N. 1998, *MNRAS*, 298, 67
- Wex, N., Kalogera, V., & Kramer, M. 2000, *ApJ*, 528, 401
- Will, C. M. 1993, *Theory and Experiment in Gravitational Physics*, (Cambridge: Cambridge University Press)